
Permeation Fill-Tube Design for Inertial Confinement Fusion Target Capsules

Introduction

In inertial confinement fusion (ICF)¹ a target capsule containing a cryogenic deuterium–tritium (DT) ice layer and low-density DT gases is imploded directly by intense laser pulses² or indirectly by x rays in a hohlraum.³ During a typical implosion, intense illumination of the target rapidly heats and ablates the outer capsule material. Conservation of momentum drives the remaining capsule material and fuel toward the center of the target sphere, where the initially gaseous fuel forms a “hot spot” that ignites fusion reactions, which propagate radially outward through the main fuel layer.³ The ultimate goal of ICF is to ignite the imploding target capsule, producing net energy gain; however, during an implosion, hydrodynamic instabilities in the ablation front can reduce the energy yield by distorting the hot spot or dispersing the main fuel layer.

Currently, two main methods are being used to fill the ICF target capsule with DT fuel—fill-tube filling⁴ and permeation filling.⁵ In fill-tube filling, a small fill tube provides a connection between the empty target capsule and a reservoir of gaseous DT. A valve downstream of the supply is opened, and DT flows into the target capsule. Once the desired amount of DT is inside the target capsule, the supply is shut off.

Permeation filling has no fill-tube connection between the empty target capsule and a reservoir of gaseous DT. Instead, this method relies on the target capsule being permeable to DT at the filling temperature and nonpermeable at some lower temperature. A valve downstream of the supply is opened and, at a controlled pressure ramp rate, DT flows into a heated pressure vessel containing an empty target capsule. The buckling strength and permeability of the target capsule shell limit the rate of DT pressure rise.⁶ Once the desired amount of DT has entered the target capsule, corresponding to the maximum DT fill pressure, the supply valve is closed. The pressure vessel and target capsule are then cooled to a temperature at which the internal pressure will not cause the target capsule to rupture or leak extensively when DT in the chamber surrounding the target capsule is evacuated.

One common capsule material (i.e., ablator) used in permeation filling is made by using the glow-discharge polymerization (GDP) process.⁷ Alternate ablators such as beryllium, silicon, and high-density carbon are of interest in ICF experiments that study hydrodynamic instabilities.⁸ Unfortunately, target capsules made of these materials are not sufficiently permeable to DT to be used in permeation filling. The current infrastructure at LLE is based on permeation filling. To study alternate ablator materials, a new cryostat design based on a fill-tube fill system is required—a multiyear, multimillion dollar project. A novel design combining the attributes of permeation and fill-tube filling is described next. This design requires no changes to LLE’s current infrastructure, which will allow the study of alternate ablator materials in cryogenic experiments to begin immediately.

Description of the Permeation Fill-Tube Design

The permeation fill-tube (PFT) target assembly is shown in Fig. 146.35, while a more detailed image of the upper portion of the assembly is shown in Fig. 146.36. The gravity vector points down in these images. The geometry of the target support is driven by the requirement that the target capsule must be at the same elevation or lower than the permeation cell, and the support structure must not interfere with the laser beams.

Figure 146.37 shows a typical PFT assembly. The permeation cell is connected to the target capsule by a fill tube with adhesive joints. The fill tube itself is made of two separate tubes that are also glued together. The larger-diameter tube is fused silica with an outer polymeric coating and has an outer diameter (OD) of 0.15 mm and inner diameter (ID) of 0.10 mm. The smaller-diameter tube is borosilicate glass and is tapered from an OD of 0.1 mm and ID of 0.080 mm to an OD of 0.030 mm and ID of 0.022 mm. Smaller diameters for fill tubes will be investigated in the future. The initial geometry was chosen because of its high rigidity and strength for initial filling and layering experiments.

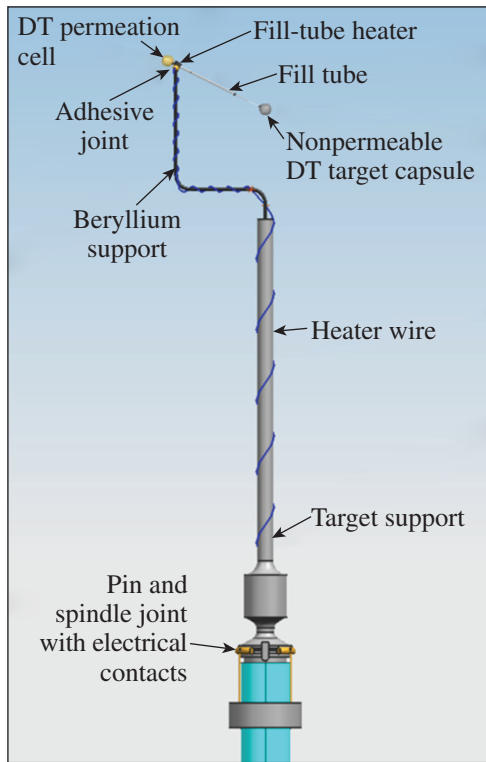
The PFT method combines attributes of fill-tube filling⁴ and permeation filling.⁶ Here the target capsule is nonpermeable to

DT while the permeation cell is permeable to DT at the filling temperature and nonpermeable at some lower temperature. A valve downstream of the supply is opened and, at a controlled pressure ramp rate, DT flows into a heated pressure vessel con-

taining an empty PFT target assembly (shown in Fig. 146.35). The buckling strength and permeability of the target capsule shell limit the rate of DT pressure rise.⁶ DT flows through the permeation cell's shell through the fill tube and into the target capsule. At a steady state the gas pressure is equal in both capsules. Once the desired amount of DT has entered the PFT assembly, corresponding to the maximum DT fill pressure, the supply valve is closed. The pressure vessel and the PFT target assembly are then cooled to a temperature at which the internal assembly's pressure will not cause the target capsule or the permeation cell to rupture or leak appreciably when DT in the chamber surrounding the PFT assembly is finally evacuated.

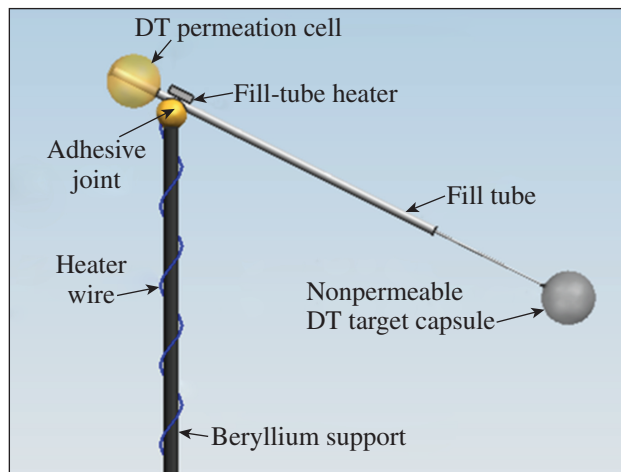
The heater glued to the fill tube (shown in Figs. 146.35 and 146.36) is a microchip resistor (ERJ-XGNF1-1Y) capable of delivering up to ~1 mW. The heater creates a pressure delta to drive more fuel into the target capsule than the permeation cell during the layering process. Without this heater, the pressures in the target capsule and the permeation cell would be equal.

The initial PFT prototype did not use nonpermeable ablaters, such as beryllium, silicon, and high-density carbon (HDC), since, because of their opacity to visible light, the ice layers would not have been visible. LLE uses optical backlit shadowgraphic characterization of cryogenic target ice layers with submicron resolution.⁹ The initial PFT assembly with a HDC target capsule, used for our manufacturing studies, is shown in Fig. 146.38(a). The PFT assembly in our layering studies used GDP capsules for both the permeation cell and the



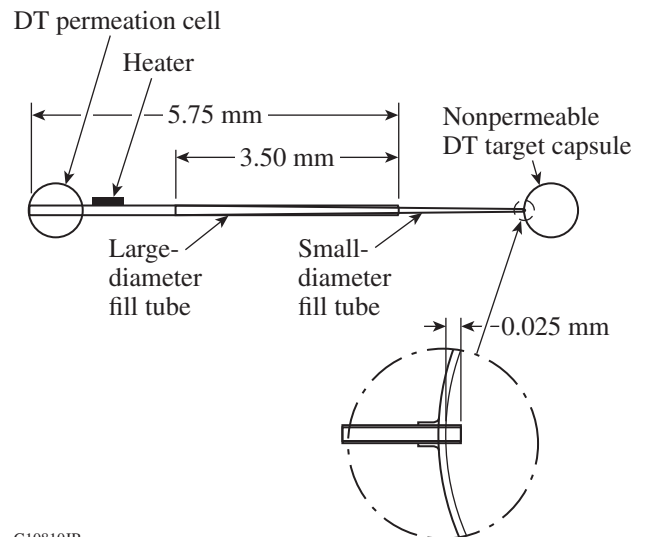
G10808JR

Figure 146.35
Permeation fill-tube target assembly. DT: deuterium-tritium.



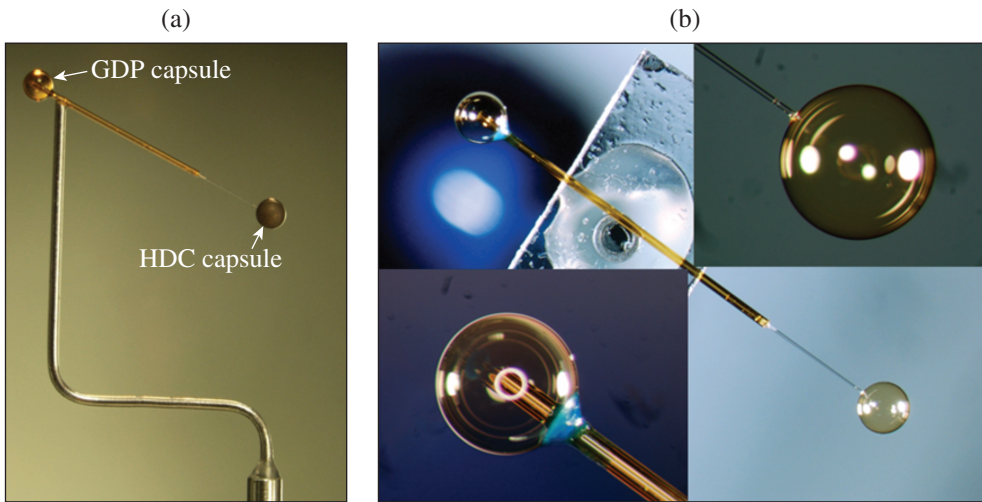
G10809JR

Figure 146.36
Detailed view of the upper portion of a permeation fill-tube target assembly.



G10810JR

Figure 146.37
Permeation fill-tube assembly. (All dimensions are in millimeters.)



G10811JR

Figure 146.38

(a) Image of a PFT target assembly with a glow-discharge polymerization (GDP) permeation cell and high-density carbon (HDC) nonpermeable target capsule; (b) image of a PFT assembly with a GDP permeation cell and GDP target capsule.

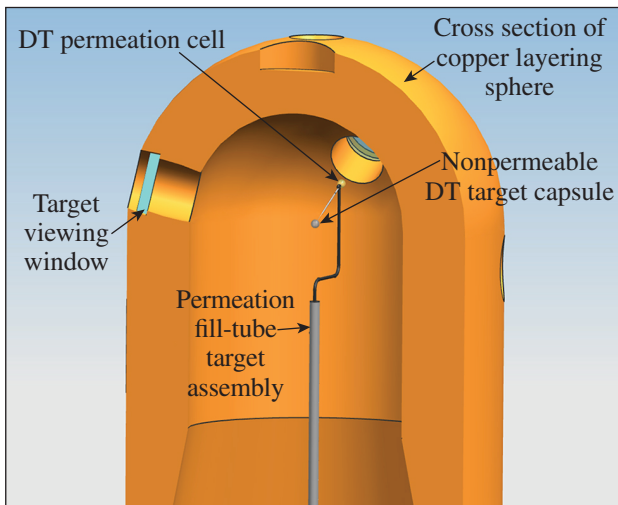
target capsule [see Fig. 146.38(b)]. The target capsule was made from GDP so the ice layer would be visible for layering studies. Both capsules had an OD of 0.430 mm, with wall thicknesses of 0.022 and 0.008 mm for the permeation cell and the target capsule, respectively. A future fill will use a nonpermeable multilayer (GDP/Si/GDP) target capsule shell.

PFT Layering Process

The PFT assembly is located inside a copper layering sphere filled with helium (see Fig. 146.39). Initially DT in the PFT assembly is rapidly cooled (~1 K/s) to several degrees below its triple point. Next, the temperature of the copper layering sphere is gradually raised until all of the solid DT in the target capsule is gone and the solid DT in the fill-tube section nearest

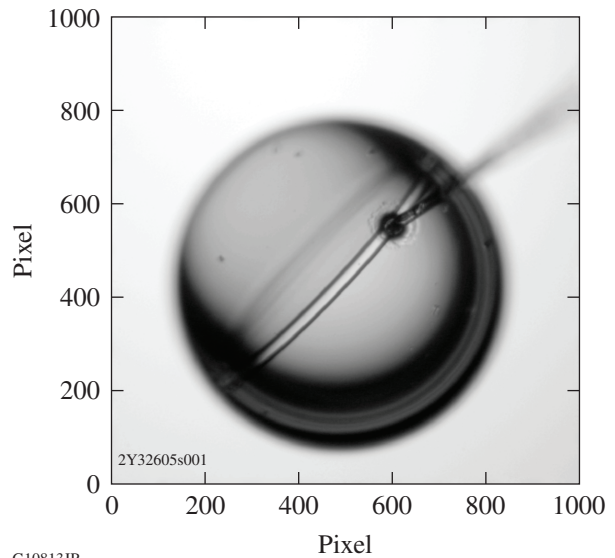
the target capsule begins to melt. At this point the temperature of the layering sphere is dropped ~0.001 mK every 15 min. This causes the DT to solidify and an ice crystal “seed” to grow out of the fill tube into the target capsule. The initial growth of a single ring (shown in Fig. 146.40) indicates that, as the temperature continues to drop, the final ice layer will contain a single hexagonal close-packed (hcp) crystal, as required for high-yield ICF implosions.¹⁰

Layering experiments were successful using the same layering protocol as existing stalk-mounted (non-fill-tube)



G10812JR

Figure 146.39
PFT assembly located inside a copper layering sphere.



G10813JR

Figure 146.40
Image of single crystal seed that grows out of the fill tube. The initial growth of a single ring is indicative of a final ice layer that will be composed of a single hexagonal close-packed (hcp) crystal, which is required for high-yield ICF implosions.¹⁰

targets. An image of the resulting single-hcp-crystal ice layer characterized by optical backlit shadowgraphy is shown in Fig. 146.41(a). The inner ice surface roughness is $0.98\text{-}\mu\text{m}$ rms (root mean square) and the average ice thickness is $61\ \mu\text{m}$. Figure 146.41(b) shows the inner ice surface radius in red and outer ice surface radius in blue. The difference between the blue curve and the red curve is the ice thickness. (A smaller radius of the inner ice surface, shown in red, corresponds to a thicker ice layer.) The image is unwrapped with the zero position referring to the 3:00 position in Fig. 146.41(a). The stalk position is $\sim 50^\circ$, leading to thick ice near the fill tube (highlighted). The test ice layer is significantly thicker near the

fill tube because of the higher ($\sim 6\times$) thermal conductivity of borosilicate glass compared to helium. From Fig. 146.41(b) it appears that the maximum variation in ice thickness near the fill tube is $\sim 7\ \mu\text{m}$, but it is actually larger because the fill tube obscures the shadowgraph data, causing the image analysis to fail in this area. From Fig. 146.41(b), the effect of the fill tube is seen over $\sim \pm 23^\circ$ on either side of the fill tube. The thick spot will be discussed further in the next section.

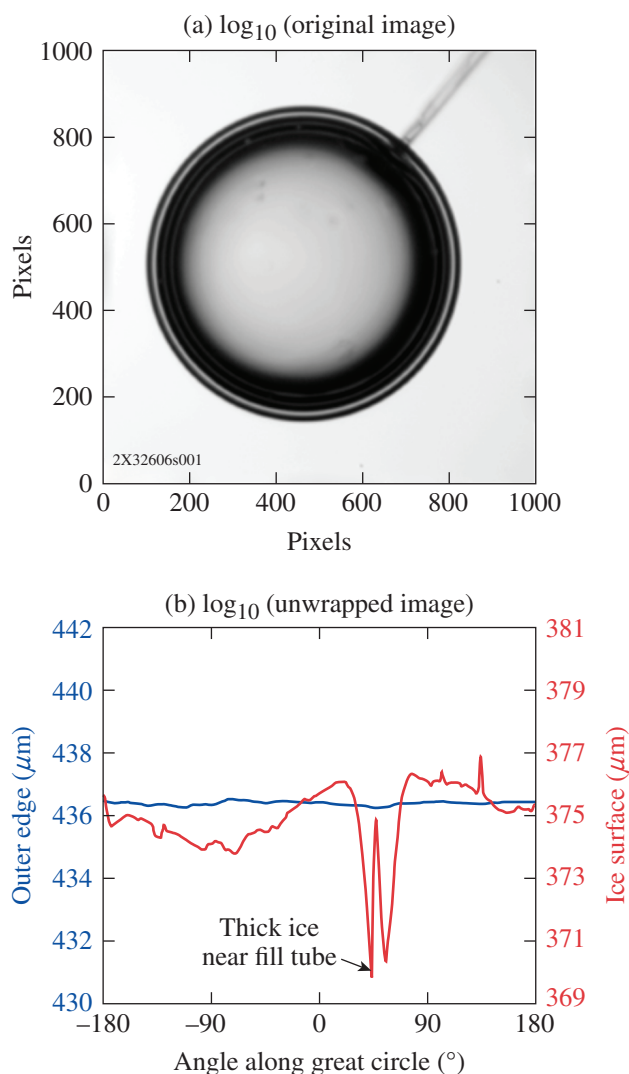
It is possible to control the relative pressure of DT in the two capsules by using the PFT heater located near the permeation cell shown in Fig. 146.36. With the heater turned on ($\sim 1\ \text{mW}$) and the layering-sphere temperature above the critical point of DT, $\sim 40\ \text{K}$, gas is preferentially driven toward the target capsule. Next, the DT in the layering sphere is rapidly cooled ($\sim 1\ \text{K/s}$) several degrees below DT's triple point, causing the DT in the target capsule and the fill tube's end attached to the target capsule to freeze. At this point the PFT heater is turned off and the layering process described previously can begin. As long as the ice plug remains in the fill tube during the subsequent layering process, the amount of DT in the target capsule will remain constant.

Heat-Transfer Model

It is preferable to use a heat-transfer model to investigate the effects of the fill tube, glue spot, target capsule geometry, and material properties on layer-thickness uniformity for PFT ICF targets. If the layer-thickness uniformity of the current design can be accurately modeled, we are confident that we will be able to numerically evaluate future ICF target designs. Using models to design targets is more efficient than building physical prototypes.

The DT solid/gas phase boundary is represented by an isotherm at DT's triple point of $\sim 19.7\ \text{K}$. The PFT temperature profile was modeled by a finite volume method (FVM) using ANSYS *FLUENT* v16. A two-dimensional axisymmetric model of the PFT target assembly inside a 1-in.-diam copper layering sphere filled with ~ 2 Torr of helium was constructed. The model includes both capsules, the fill tube, the glue spot connecting the target capsule to the fill tube, DT decay heating, and sublimation/deposition of DT in the permeation cell, fill tube, and target capsule. The layering sphere was treated as a complete surface and is represented by a uniform-temperature boundary condition. Holes in the layering sphere were ignored so a computationally efficient axisymmetric model can be used.

Decay heating of DT causes the target to be hotter than its surroundings. Helium was used to conduct the heat generated



G10814JR

Figure 146.41
(a) An image of a final single hcp crystal ice layer characterized by optical backlit shadowgraphy; (b) the inner ice surface radius is shown in red and the outer ice surface radius in blue.

by DT to the surrounding copper sphere. In the model, DT can exist in only one of two phases—solid or gaseous. The sublimation/deposition temperature used for DT was 19.7 K. Initial models used *FLUENT*'s two-phase routines. Since only steady-state results were of interest, a more-efficient solution procedure was developed. Using user-defined DT material properties (density and conductivity) that were a function of temperature yielded identical steady-state results as *FLUENT*'s two-phase routine and were more efficient to run. Both solution procedures model only heat transfer by conduction, and mass conservation is not automatically taken into account. In either modeling method, conservation of DT mass is controlled by a manual iterative process. Knowing the actual total mass of DT in the PFT assembly, the layering sphere's fixed-temperature boundary condition can be adjusted until the desired mass of DT contained in the PFT assembly is obtained.

Figure 146.42 shows the model geometry. The outer portion of the DT physically touching the target capsule shell uses a cell size of $1 \times 1 \mu\text{m}$ to resolve the gas/ice-phase boundary (shown in Fig. 146.43). Other areas of the model use a coarser mesh for a more-efficient solution. Based on a mesh refinement study, the results presented are mesh independent. Thermal conductivities at $\sim 20 \text{ K}$ are 0.0255, 0.009, 0.35, 0.05, 0.333, 0.15, 0.15, and 59 W/m/K for He (Ref. 11), DT gas,¹² DT solid,¹² GDP plastic shell,¹³ Stycast 1266 (Ref. 14), fused silica,¹⁵ borosilicate glass,¹⁵ and beryllium,¹⁶ respectively. Densities are 0.0065, 0.7, 260, 1420, 1120, 2640, 2640, and 1851 kg/m³ for He, DT gas, DT solid, GDP plastic shell, Stycast 1266, fused silica, borosilicate glass, and beryllium, respectively. A user-defined function (UDF) was used for the 200-W/kg decay heat of DT (Ref. 13). (Note: Borosilicate glass conductivity was used for fused silica and polyimide conductivity was used for the GDP capsule because of the lack of cryogenic material property data.)

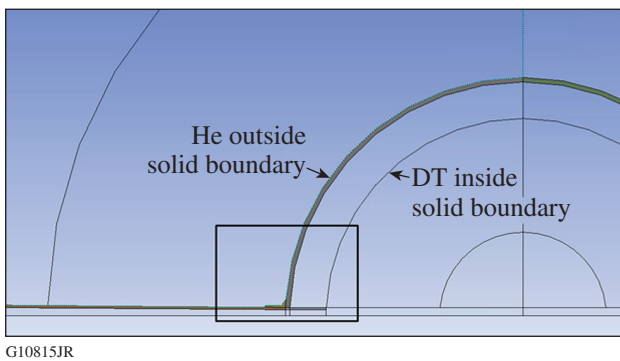


Figure 146.42
Model geometry near the target capsule.

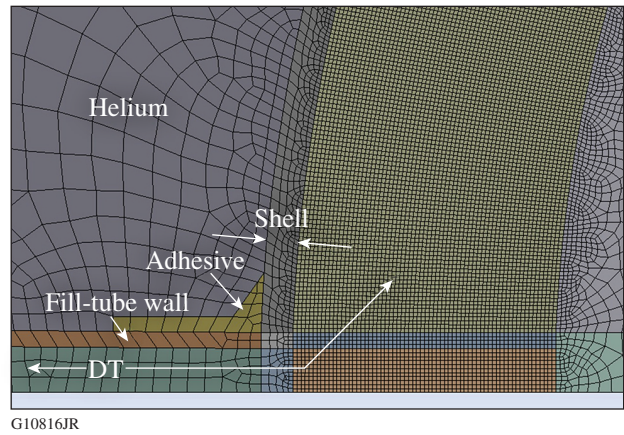


Figure 146.43
Image of the fine mesh required to resolve the solid/gas phase boundary near the target capsule.

Figure 146.44 shows temperature contours predicted by the model. The temperature is hottest at the center of the target (radioactive decay) and coldest at the isothermal boundary condition representing the copper layering sphere. Figure 146.45 illustrates the resulting solid/gas phase boundary predicted by the model (DT ice is shown in red). Figure 146.46 is an unwrapped image of the model ice thickness overlaid on the measured ice thickness of the layer in the experimental PFT target; the fill tube is located at $\sim 50^\circ$. The model thickness profile is very similar to experimental results. One difference is that the actual ice layer shows a thick spot in the ice above the hole in the layering sphere (required to insert the target

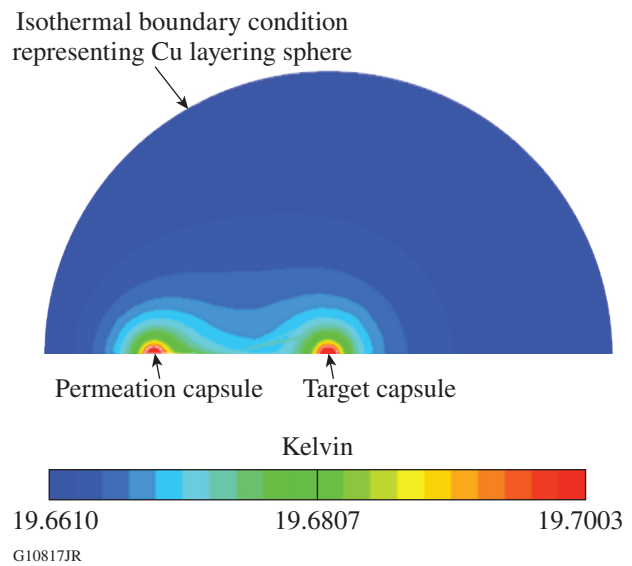


Figure 146.44
Modeled temperature contours of the target and copper layering sphere.

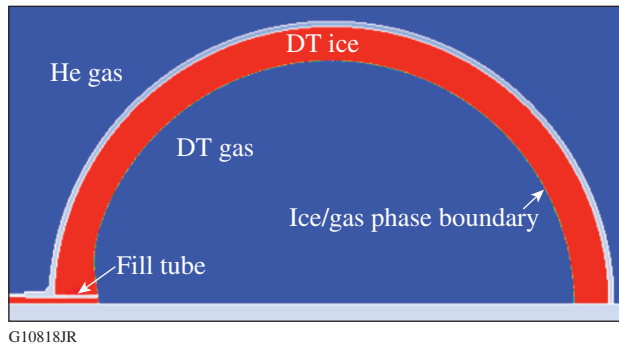


Figure 146.45
The ice/gas phase boundary predicted by the model (DT ice is shown in red).

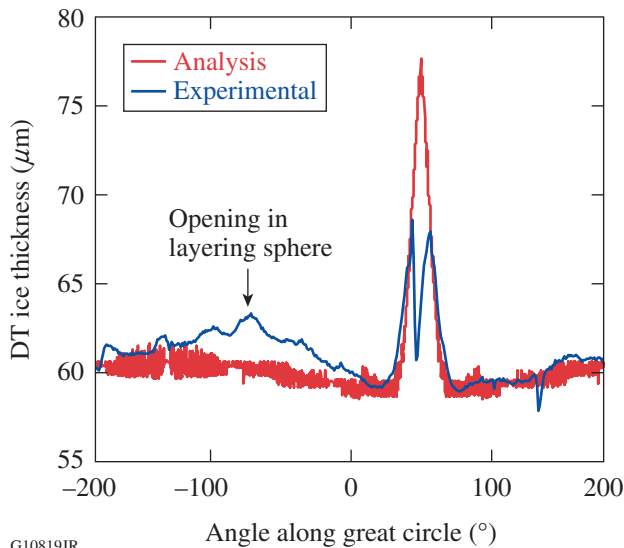


Figure 146.46
Unwrapped image of the model prediction of ice thickness overlaid on actual ice thickness; the fill tube is located at $\sim 50^\circ$.

into the layering sphere). The hole cannot be modeled since the axis for the axisymmetric model is aligned with the fill tube. The thermal model estimates the peak thickness variation to be $\sim 17 \mu\text{m}$ near the fill tube, and the effect of the fill tube is apparent $\sim \pm 20^\circ$ on either side. The model accurately predicts the uniformity of the actual ice-layer thickness. This verifies the modeling methodology so good estimates of ice uniformity for other ICF target designs can be made numerically.

The nonuniformity in the ice thickness near the fill tube for the target design discussed above is too large for high-yield ICF implosions. Three critical design parameters affecting this nonuniformity are (1) the fill tube’s size, (2) the target shell’s thermal conductivity, and (3) the fill tube’s thermal conductivity. The decay heat from the target is conducted (radially) away

from the target shell. Nonuniformities in this conduction path distort the isotherms, resulting in ice-thickness nonuniformity. If the isotherms were perfectly concentric about the target shell, the ice thickness would be uniform. The thermal conductivity of borosilicate glass is $\sim 6\times$ higher than helium, causing a cold spot near the fill tube that results in locally thicker ice. Minimizing the borosilicate glass cross-sectional area or its thermal conductivity will minimize this effect. Less obvious is the effect of shell conductivity on ice-thickness uniformity. The fill-tube causes temperature variations in the θ direction in the axisymmetric model, resulting in nonconcentric isotherms. When the shell has high thermal conductivity, it “short circuits” the θ temperature variations, resulting in more-concentric isotherms.

Here we use the model to quantify the effect of alternate target designs on ice-layer nonuniformities near the fill tube. First we investigate the effect of a fill tube’s cross-sectional area on the ice-thickness uniformity near the fill tube. The effect of borosilicate fill-tube size on ice-thickness uniformity with a GDP (low thermal conductivity of 0.05 W/m/K) shell is shown in Fig. 146.47. The fill-tube size has a significant effect on variations in ice-layer thickness near the fill tube. The variation decreases from $\sim 30\%$ for the $30\text{-}\mu\text{m-OD}$ fill tube to $\sim 10\%$ for the $10\text{-}\mu\text{m-OD}$ fill tube.

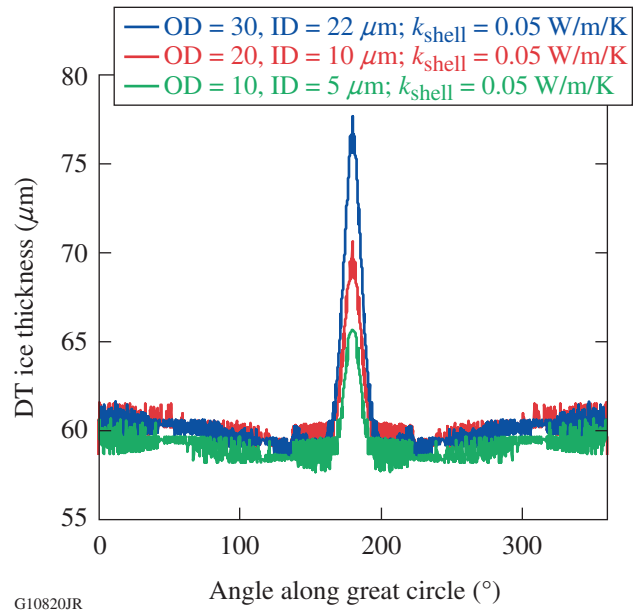


Figure 146.47
Unwrapped image of the model prediction of ice thickness for three different fill-tube cross sections with a GDP shell having a thermal conductivity of 0.05 W/m/K .

The effect of the shell's thermal conductivity for a 20- μm -OD, 10- μm -ID borosilicate fill tube with 20 μm of penetration into the shell is shown in Fig. 146.48. The shell's thermal conductivity has a significant effect on variations in ice-layer thickness near the fill tube. Bulk beryllium at ~ 20 K has a thermal conductivity of ~ 59 W/m/K. If a target shell has a thermal conductivity approaching that of bulk beryllium, it would almost completely negate the ice-thickness variations near the fill tube.

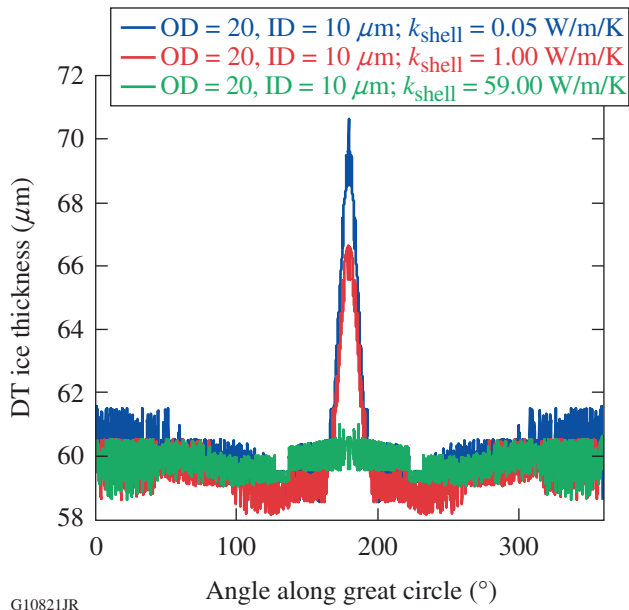


Figure 146.48
Unwrapped image of the model prediction of ice thickness for three different shell thermal conductivities with a 20- μm OD, 10- μm ID borosilicate fill tube.

Conclusions

An ICF target has been successfully filled and a <1 - μm -rms DT ice layer has been developed using a novel fill design that combines attributes of permeation and fill-tube filling. This new filling method allows LLE to immediately begin the study of nonpermeable cryogenic target capsules with their current infrastructure. A numerical model has been presented that accurately predicts the ice nonuniformities near the fill tube as seen in empirical data. Using this model, target designs with better ice-thickness uniformity have been proposed. One key but less obvious factor that improves ice uniformity is the target shell's conductivity. Numerical simulations show that high-conductivity shells (e.g., shells with the conductivity of bulk beryllium at ~ 20 K, 59 W/m/K) completely negate the fill-tube-induced ice nonuniformities.

ACKNOWLEDGMENT

This material is based upon work supported by the Department of Energy National Nuclear Security Administration under Award Number DE-NA0001944, the University of Rochester, and the New York State Energy Research and Development Authority. The support of DOE does not constitute an endorsement by DOE of the views expressed in this article.

REFERENCES

1. J. Nuckolls *et al.*, *Nature* **239**, 139 (1972).
2. R. L. McCrory, D. D. Meyerhofer, R. Betti, R. S. Craxton, J. A. Delettrez, D. H. Edgell, V. Yu. Glebov, V. N. Goncharov, D. R. Harding, D. W. Jacobs-Perkins, J. P. Knauer, F. J. Marshall, P. W. McKenty, P. B. Radha, S. P. Regan, T. C. Sangster, W. Seka, R. W. Short, S. Skupsky, V. A. Smalyuk, J. M. Soures, C. Stoeckl, B. Yaakobi, D. Shvarts, J. A. Frenje, C. K. Li, R. D. Petrasso, and F. H. Séguin, *Phys. Plasmas* **15**, 055503 (2008).
3. J. D. Lindl, *Phys. Plasmas* **2**, 3933 (1995).
4. D. E. Solomon and T. M. Henderson, *J. Phys. D: Appl. Phys.* **8**, L85 (1975).
5. S. O. Kucheyev and A. V. Hamza, *J. Appl. Phys.* **108**, 091101 (2010).
6. *LLE Review Quarterly Report* **81**, 6, Laboratory for Laser Energetics, University of Rochester, Rochester, NY, LLE Document No. DOE/SF/19460-335 (1999).
7. A. Nikroo *et al.*, General Atomics, San Diego, CA, Report GA-A23881 (2002).
8. A. J. MacKinnon, N. B. Meezan, J. S. Ross, S. Le Pape, L. Berzak Hopkins, L. Divol, D. Ho, J. Milovich, A. Pak, J. Ralph, T. Döppner, P. K. Patel, C. Thomas, R. Tommasini, S. Haan, A. G. MacPhee, J. McNaney, J. Caggiano, R. Hatarik, R. Bionta, T. Ma, B. Spears, J. R. Rygg, L. R. Benedetti, R. P. J. Town, D. K. Bradley, E. L. Dewald, D. Fittinghoff, O. S. Jones, H. R. Robey, J. D. Moody, S. Khan, D. A. Callahan, A. Hamza, J. Biener, P. M. Celliers, D. G. Braun, D. J. Erskine, S. T. Prisbrey, R. J. Wallace, B. Kozioziemski, R. Dylla-Spears, J. Sater, G. Collins, E. Storm, W. Hsing, O. Landen, J. L. Atherton, J. D. Lindl, M. J. Edwards, J. A. Frenje, M. Gatu-Johnson, C. K. Li, R. Petrasso, H. Rinderknecht, M. Rosenberg, F. H. Séguin, A. Zylstra, J. P. Knauer, G. Grim, N. Guler, F. Merrill, R. Olson, G. A. Kyrala, J. D. Kilkenny, A. Nikroo, K. Moreno, D. E. Hoover, C. Wild, and E. Werner, *Phys. Plasmas* **21**, 056318 (2014).
9. D. H. Edgell, W. Seka, R. S. Craxton, L. M. Elasky, D. R. Harding, R. L. Keck, M. Pandina, M. D. Wittman, and A. Warrick, presented at the 46th Annual Meeting of the Division of Plasma Physics, Savannah, GA, 15–19 November 2004.
10. T. C. Sangster, R. Betti, R. S. Craxton, J. A. Delettrez, D. H. Edgell, L. M. Elasky, V. Yu. Glebov, V. N. Goncharov, D. R. Harding, D. Jacobs-Perkins, R. Janezic, R. L. Keck, J. P. Knauer, S. J. Loucks, L. D. Lund, F. J. Marshall, R. L. McCrory, P. W. McKenty, D. D. Meyerhofer, P. B. Radha, S. P. Regan, W. Seka, W. T. Shmayda, S. Skupsky, V. A. Smalyuk, J. M. Soures, C. Stoeckl, B. Yaakobi, J. A. Frenje, C. K. Li, R. D. Petrasso, F. H. Séguin, J. D. Moody, J. A. Atherton, B. D. MacGowan, J. D. Kilkenny, T. P. Bernat, and D. S. Montgomery, *Phys. Plasmas* **14**, 058101 (2007).

11. N. B. Vargaftik *et al.*, *Handbook of Thermal Conductivity of Liquid Gases* (CRC Press, Boca Raton, FL, 1994)
12. P. C. Souers, *Hydrogen Properties for Fusion Energy* (University of California Press, Berkeley, CA, 1986).
13. Material Properties: Polyimide (Kapton), http://cryogenics.nist.gov/MPropsMAY/Polyimide%20Kapton/PolyimideKapton_rev.htm (24 May 2016).
14. S. Laumann *et al.*, *J. Mater. Res.* **26**, 1861 (2011).
15. Thermal and Mechanical Properties of Glass (Quartz, Pyrex, Borosilicate), <http://www.yutopian.com/Yuan/prop/Glass.html> (24 May 2016).
16. Be Properties, <https://www.bnl.gov/magnets/staff/gupta/cryogenic-data-handbook/Section7.pdf> (24 May 2016).